Balloon-borne observations of short vertical wavelength gravity waves and interaction with QBO winds

R. A. Vincent[1]*, **M. J. Alexander**[2]

[1]Physics, School of Physical Sciences, University of Adelaide, Adelaide, SA 5005, Australia

[2]Northwest Research Associates, CoRA Office, 3380 Mitchell Lane, Boulder, CO 80301, USA

Key Points:

- Combined superpressure balloon and radiosonde observations are used to study inertia-gravity waves at the equator
- Eastward and westward wave packets with 1 and 3 day periods are identified and momentum fluxes computed
- Contributions to the QBO are substantial for the short event periods considered.

*Physics, School of Physical Sciences, University of Adelaide, Adelaide, SA 5005, Australia

Corresponding author: M. Joan Alexander, alexand@nwra.com

Abstract

The quasi-biennial oscillation (QBO), a ubiquitous feature of the zonal mean zonal winds in the equatorial lower stratosphere, is forced by selective dissipation of atmospheric waves that range in periods from days to hours. However, QBO circulations in numerical models tend to be weak compared with observations, probably because of limited vertical resolution that cannot adequately resolve gravity waves and the height range over which they dissipate. Observations are required to help quantify wave effects. The passage of a superpressure balloon (SPB) near a radiosonde launch site in the equatorial Western Pacific during the transition from the eastward to westward phase of the QBO at 20 km permits a coordinated study of the intrinsic frequencies and vertical structures of two inertia-gravity wave packets with periods near 1-day and 3 days, respectively. Both waves have large horizontal wavelengths of about 970 and 5500 km. The complementary nature of the observations provided information on their momentum fluxes and the evolution of the waves in the vertical. The near 1-day westward propagating wave has a critical level near 20 km, while the eastward propagating 3-day wave is able to propagate through to heights near 30 km before dissipation. Estimates of the forcing provided by the momentum flux convergence, taking into account the duration and scale of the forcing, suggests zonal force of about 0.3-0.4 $ms^{-1}day^{-1}$ for the 1-day wave and about 0.4-0.6 $ms^{-1}day^{-1}$ for the 3-day wave, which acts for several days.

1 Introduction

Tropical gravity waves play a major role in driving tropical circulation above the tropopause. In particular, the tropical quasi-biennial oscillation (QBO) in zonal mean zonal winds of the lower stratosphere is primarily driven by dissipation of gravity waves, and a growing body of evidence shows the phase of the QBO to be important to climate prediction at sub-seasonal to interannual timescales (Boer & Hamilton, 2008; Scaife et al., 2014; Smith et al., 2016; Marshall et al., 2017; Garfinkel et al., 2018; Lim et al., 2019). As a result, there is an increasing effort to simulate a realistic QBO in global models, and this is currently achieved through parameterization of non-orographic gravity wave drag (Kawatani & Hamilton, 2013; Butchart et al., 2018). Unfortunately, the QBO tends to be a weaker source of predictability in the models than observations suggest it to be (M. J. Alexander & Holt, 2019), and limitations in fidelity of model representations of

the QBO may be responsible. This puts a special emphasis on better understanding of tropical gravity waves and their interactions with the QBO.

A major reason that modeled QBO circulations are weak in the lower stratosphere is because parameterized gravity wave drag tends to be weaker there than at upper levels near 10 hPa ($\sim$ 30 km) . Weaknesses in gravity wave parameterization methods may be partly to blame. Evidence suggests that increasing model vertical resolution improves the simulation of the QBO (Giorgetta et al., 2002; Richter et al., 2014), because resolved tropical wave drag increases at higher vertical resolution (Holt et al., 2016, 2020). These resolved waves may include Kelvin waves, mixed Rossby-gravity waves, and inertia-gravity waves. If vertical resolution is too coarse, these resolved large-scale waves will dissipate at altitudes well below their critical levels, which could lead to consistently weaker forces on the mean flow in models than in the real atmosphere. Precisely how closely waves of all horizontal scales approach their critical levels before dissipating is therefore a significant source of uncertainty in modeling the QBO.

As waves propagate vertically and approach their critical levels in QBO shear, their phase speeds c_0 approach the wind speed $U(z)$. The Kelvin and gravity wave dispersion relation, for example,

$$m = Nk_h/(U - c_o), \tag{1}$$

tells us that the vertical wavelength $\lambda_z = 2\pi/|m|$ shrinks in proportion to the intrinsic phase speed $|U-c_0|$. Here, N is the Brunt-Vaisala frequency, and k_h is the horizontal wavenumber. While dispersion relations differ in detail for other tropical waves, λ_z still shrinks as the waves approach critical levels, and without very high vertical resolution, model diffusion may eliminate a wave far below its critical level. This is important to the force imparted to the mean flow when the wave dissipates because momentum flux F_M is constant for waves propagating without dissipation, while the drag force D occurs with dissipation of F_M given by,

$$D = -\frac{1}{\rho}\frac{dF_M}{dz}. \tag{2}$$

If, due to coarse vertical resolution, the wave dissipates several km lower (say at $\rho(z_1)$) than it should (say at $\rho(z_2)$), the resulting force may be 50% smaller ($\rho(z_1)/\rho(z_2)$) due to the exponential decrease in density with altitude.

Fine vertically-resolved observations with global coverage are rare. Satellite measurements with the highest vertical resolution have shown tropical waves with vertical

wavelengths as short as ∼4 km, which is close to the vertical resolution limit (M. J. Alexander & Ortland, 2010; Wright et al., 2011), but the zonal resolution of these data limits the observable zonal wavelengths to at best 5000 km (S. P. Alexander et al., 2008). Although not made on a global scale, high-resolution radiosonde soundings do have a vertical resolution of $O \sim 50$ m, and such soundings have been used to study wave parameters such as vertical and horizontal wavelength, kinetic and potential energy, as well as to investigate wave sources (Tsuda et al., 1994; Allen & Vincent, 1995; Vincent & Alexander, 2000; Lane et al., 2003; Wang & Geller, 2003; Wang et al., 2005; Geller & Gong, 2010; Gong & Geller, 2010; Murphy et al., 2014).

A disadvantage of satellite and radiosonde GW observations is that the wave parameters are made in a ground-based reference frame so it is the ground-based frequency ω that is inferred. However, it is the wave frequency relative to the background wind, the intrinsic frequency $\hat{\omega}$, that determines important wave parameters (Fritts & Alexander, 2003). This limitation can be overcome by using superpressure balloon (SPB) observations. SPB float on an a constant density surface with typical altitudes in the range 16 to 20 km, depending on the balloon diameter, moving with the mean wind. In recent years, SPB measurements have been used to infer gravity and planetary wave parameters at latitudes ranging from the Arctic to the Antarctic (Vial et al., 2001; Hertzog et al., 2002; Vincent et al., 2007; Boccara et al., 2008; Hertzog et al., 2008, 2012; Podglajen et al., 2016), but to date only a few circumnavigating tropical trajectories have been analyzed (Jewtoukoff et al., 2013). The limitation of these measurements has been the lack of vertical structure information, which must be indirectly inferred (Boccara et al., 2008; Vincent & Hertzog, 2014).

High-resolution radiosondes provide complementary information to SPB, a factor which we exploit to study low-frequency tropical gravity waves at locations where balloon trajectories pass near a high-resolution radiosonde launch site. The SPB measurements provide detailed information on gravity waves as a function of intrinsic frequency, but without other meteorological data it can be difficult to put the GW measurements in context. In contrast, radiosondes provide vertical snapshots of the atmosphere including gravity waves, typically from the surface to a 25 to 30 km height range between the launch and burst heights. By combining SPB and radiosonde observations it is possible to overcome the limitations of each technique.

The advantages of combining near simultaneous observations made in both space and time are demonstrated by using observations made by an SPB and by high-resolution radiosondes in the western Pacific. This study arises from SPB measurements made in the PreConcordiasi campaign that took place in the equatorial regions in 2010 (Podglajen et al., 2014, 2016). Three SPB were launched from the Seychelles in this campaign. In particular, one balloon (SPB2) approached close to Manus Island in the Western Pacific, from which radiosondes were launched from Momote Airfield (2.05°S, 147.43°E) on a twice daily basis. We report on a case study of GW parameters determined using combined SPB and radiosonde data at a time when the closest approach of the SPB to Momote occurred. At this time the QBO was transitioning from its eastward to its westward phase in the lower stratosphere. We find two large-scale (∼970 and 5500 km) gravity wave packets with short vertical wavelengths and one these wave packets, in particular, is inferred to be approaching a critical level within 1 km of the observation height.

The paper is organised as follows. In section 2, the SPB and radiosonde observations are introduced. During the period when the SPB is closest to Momote two specific GW packets are identified and analyzed in section 3, including analyses of the GW changes with altitude appearing in the radiosonde records. Finally, in section 4 we make an estimate of the mean-flow forcing effects of these waves, and discuss the implications for future analyses of tropical superpressure balloon measurements currently underway through the Strateole-2 project.

2 Observations

2.1 Superpressure Balloon Observations

Superpressure balloons (SPB) are closed, inextensible, spherical envelopes filled with a fixed amount of gas. SPB ascend after launch until they reach a level where the balloon density matches the atmospheric density and then float on this isopycnic surface under the influence of the horizontal winds, acting as a quasi-Lagrangian tracer. Using GPS measurements of horizontal and vertical position with a time resolution of minutes means that the full GW spectrum can be observed. During the PreConcordiasi campaign, three 12-m diameter SPB were deployed by the Centre National d'Etudes Spatial (CNES) from the Seychelles between February and May 2010. Each balloon drifted on a constant density surface ($\rho_o \sim 0.1$ kgm^{-3}), with two SPB circumnavigating the globe within a

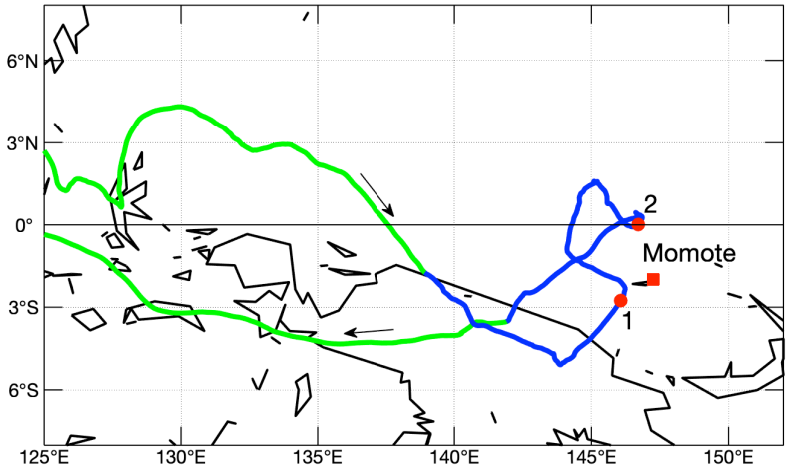

Figure 1. The green/blue line is the trajectory of SPB2 during the PreConcordiasi campaign in the period 9 April to 8 May 2010 (day of year (DoY) 99 to 128). The blue section shows the path from -2 to +4 days around the time of closest approach (DoY 117.5∼12 UT on 27 April) to Momote (red square). The red circles labelled 1 and 2 denote the central locations of two wave packets (see Section 3.1 for details).

±15° band around the equator. The trajectories are shown in Podglajen et al. (2014). The balloons carried GPS receivers to log their position and sensors to measure pressure and temperature with an overall time resolution of 1 min (see Vincent and Hertzog (2014) for details of the instruments and their accuracy).

Here we focus on the flight of SPB2, which flew at a mean altitude of 19.4±0.1 km ($\overline{p} = 63.4 \pm 1$ hPa) between 19 February and 8 May 2010. In the early part of April it moved eastward under the influence of the prevailing winds, but about 15 April the winds at the float level made a transition to westward flow as the winds associated with the quasi-biennial oscillation (QBO) descended from the middle stratosphere. Figure 1 shows the trajectory in the period from 9 April to 8 May 2010, with the blue section highlighting the trajectory in the 6-day period when the balloon was closest to Momote.

2.2 Radiosonde Observations

Radiosondes were launched twice daily (00 and 12 UT) from Momote Airfield on Manus Island (Long, 2015). Using Vaisala RS80-15GH radiosondes, pressure, temperature, dew point, wind direction and speed data were acquired every 10 s, which approx-

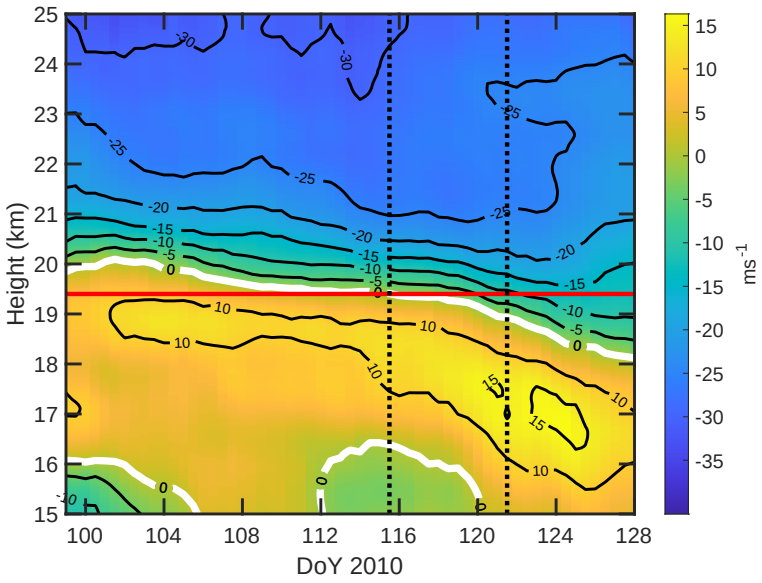

Figure 2. Cross-section of zonal winds as a function of height and day of year (DoY) constructed from seven-day moving averages of radiosonde observations made at Momote. The period covered is from 9 April to 8 May 2010. The red line shows the mean height of SPB2 (19.4 km), while the dotted lines indicate the 6-day interval centered around the date of closest approach of SPB2 to Momote (DoY 117.5).

imated to height intervals that varied from less than 10 m to about 50 m depending on the balloon ascent rate. For the purposes of this work the data were spline interpolated onto a uniform 30 m height grid. The upper levels attained varied, but usually exceeded 25 km. To ensure a uniform dataset, the upper limit here was restricted to 25 km. The mean zonal wind ($\overline{u}$) as a function of time and height is shown in Figure 2. Short term variations are reduced by using 7-day moving averages of $\overline{u}$. It is apparent that during the interval shown in Fig. 2 that the stratospheric winds at the SPB float level changed systematically from about 5 ms^{-1} eastward to 12 ms^{-1} westward as the westward phase of the QBO descended. Meridional winds were variable and weak and are not shown. For reference, the average northward speed between locations 1 and 2 shown in Fig. 1 was about 2-3 ms^{-1}.

Ambient factors that influence GW propagation in the vertical during the interval from day of year (DoY) 115.5 to 121.5 (25 April to 1 May 2010) are shown in Figure 3. The mean zonal wind profile is displayed in Fig 3a, while Figs 3b,c show the mean

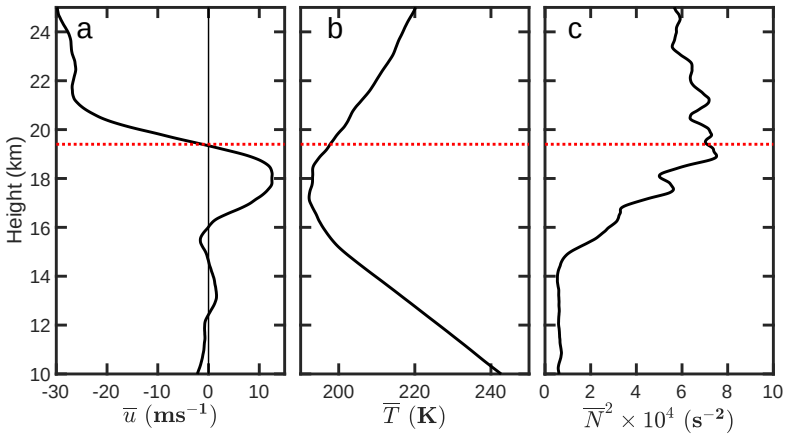

Figure 3. Vertical profiles of (a) zonal wind ($\overline{u}$), (b) temperature ($\overline{T}$) and (c) $\overline{N}^2$. Each profile is an average from radiosonde flights between DoY 115.5 and 121.5. In order to emphasize the mean structure, the $\overline{N}^2$ profile has been smoothed by a 1-km wide running mean.The red dashed lines indicate the mean flight altitude of SPB2.

temperature and the square of the Brunt-Vaisala (BV) frequency, N^2, respectively. The latter is defined as

$$N^2 = \frac{g}{\overline{T}}\left(\frac{g}{c_p} + \frac{d\overline{T}}{dz}\right) \tag{3}$$

where g is the acceleration due to gravity, $\overline{T}$ and $d\overline{T}/dz$ are mean temperature and its vertical gradient and c_p is the specific heat at constant pressure. At the float altitude $N^2 \sim 7.23\,10^{-4}$ s^{-2}, (i.e a BV period of ~ 234 sec). This parameter is also important in determining the balloon response to GW (Vincent & Hertzog, 2014) and in the GW dispersion relation (Fritts & Alexander, 2003)

$$m^2 = \frac{N^2 - \hat{\omega}^2}{\hat{\omega}^2 - f^2}k_h^2 - \frac{1}{4H^2}, \tag{4}$$

where m and k_h are the vertical and horizontal wavenumbers, f is the inertial frequency and H is the density scale height. At Momote, $f \sim 5.1 \times 10^{-6}$s^{-1} ($\tau_f \sim 14$ day).

3 Gravity Wave Case Studies

3.1 SPB Observations

To study GW, the SPB data were high-pass filtered with a 10-day cut-off to remove mean wind effects. Prior to analysis the raw float height data were checked for sudden decreases from the notional 19.4 km float altitude caused by passage across high, cold,

clouds which cause changes in the internal balloon temperature and pressure. During the 6-day period of closest approach to Momote, sudden height decreases of up to about 400 m occurred on days 115, 116 and 122, with the maximum duration being between 9.6 and 14.4 UT on day 116. The other events had durations no longer than one to two hours. Since these height changes affect the pressure, temperature and wind measurements because of the vertical gradients in the quantities, the relevant data were interpolated over and do not materially affect our studies since we are focussed on waves with periods longer than about 1 day.

Previous SPB studies show that GW effects are packet-like (Vincent et al., 2007; Boccara et al., 2008; Hertzog et al., 2008). Hence, the SPB data were analyzed using S-transforms, which decomposes the data in time-frequency space (Stockwell et al., 1996), akin to the Morlet wavelet methodology used in the studies cited above. The S-transform basis functions are formed as the product of sinusoidal functions modulated by a Gaussian with width inversely proportional to the frequency. The temporal integral of the S-transform gives the Fourier transform. The Gaussian is translated along the temporal dimension to give the localization of spectral information, while the phase remains fixed relative to a single time (M. J. Alexander et al., 2008).

The S-transform spectrum of the GW total energy KE + PE,

$$E_T = \frac{1}{2}\left(u'^2 + v'^2\right) + \frac{1}{2}\left(\frac{g^2}{N^2}\frac{T'^2}{\overline{T}^2}\right), \tag{5}$$

is shown in Figure 4. T' is the GW-induced temperature perturbation, derived after removing the effect of SPB vertical displacements in the presence of the background temperature gradient (Vincent & Hertzog, 2014).

Since we are concerned with waves close to the equator (Fig. 1), where f is small, we can use the so-called medium-frequency approximation, that is GW with intrinsic frequencies in the range $N^2 >> \hat{\omega}^2 >> f^2$. A particular emphasis is on wave periods longer than 1 day, so only wave periods between 5 days and 16 hr (frequencies between 0.2 and 1.5 d^{-1}) are shown in Fig 4. This analysis revealed that there are two distinct features in the 6-day interval of interest. These spectral features, 1 and 2, are highlighted by the white boxes in Figure 4. Similar peaks at the same frequencies and times also appear in spectra of other measured parameters, such as pressure, albeit with somewhat different relative amplitudes. We conclude that these features are associated with long-period gravity waves.

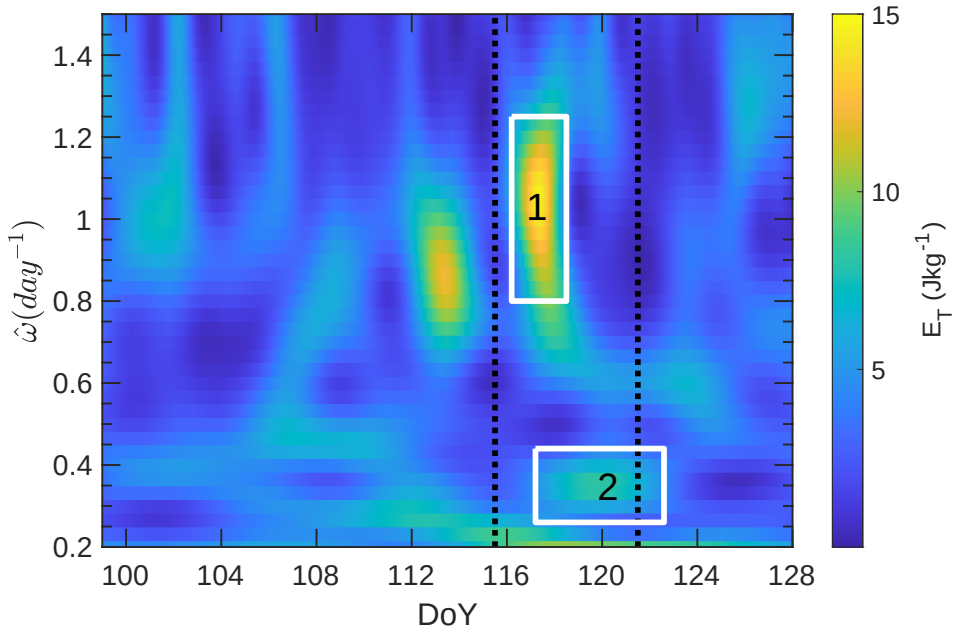

Figure 4. Time-frequency S-transform spectrum of the total energy (E_T=KE+PE) from SPB observations from DoY 99 to 128, 2010. The white boxes labelled 1 and 2 denote spectral regions that are subject to further analysis. The vertical dashed lines indicate the 6-day interval corresponding to the interval centered around the date of closest approach to Momote.

Table 1. Basic parameters associated with wave packets 1 and 2 (Fig. 4). E_{max} is the peak total energy of each packet. t_o and $\hat{\omega}$ are the respective dates and frequencies of the peak values and Δt_o and $\Delta\hat{\omega}$ are the associated *rms* widths of the spectral features. Lat. and Lon. give the latitude and longitude of the SPB position at the times of peak amplitude.

Parameter	1	2
E_{max} (Jkg^{-1})	15.1	8.23
t_o (DoY)	117.3	119.8
Δt_o (day)	0.79	2.47
$\hat{\omega}$ (d^{-1})	1.05	0.36
$\Delta\hat{\omega}$ (d^{-1})	0.20	0.07
Lat. (deg)	-2.76	0.00
Lon. (deg)	146.08	146.71

To quantify the basic parameters of the regions or 'packets' evident in Fig. 4, Gaussian functions were independently fitted in both time and frequency. The results are sum-

marized in Table 1. 'Packet' 1 is of short duration, with a width ($2\times\Delta t_o$) of about 1.6 days and an associated wide spread in frequency (0.40 d^{-1}). The corresponding values for 'packet' 2 are ~5 days and 0.14 d^{-1}, respectively. The intrinsic periods for 1 and 2 are 0.95 (0.87-1.33) days, and 2.77 (2.33-3.44) days, where the values in brackets denote the 95% uncertainties derived from the Gaussian fitting parameters.

With respect to packet 1, which has a period close to one day, it should be noted that there is a diurnal deviation from isopycnic behavior associated with expansion of the balloon envelope due to solar heating (Podglajen et al., 2016). However, the vertical displacements associated with this particular event are many times the amplitude of the solar heating effect and the phase of the oscillation is in anti-phase/quadrature with that expected for the sunrise/sunset cycle. We conclude that the solar heating effect is not relevant in this particular case.

It is now straightforward to obtain the relevant wave parameters following the analysis outlined in section 5 of Vincent and Hertzog (2014), with some modifications. Briefly, for each packet the perturbation wind field was rotated through an angle θ required to maximize the value of $U_{||}$, the modulus of the horizontal wind perturbation. This gives the horizontal direction of travel with an ambiguity of $\pm 180°$. The intrinsic phase speed $\hat{c}$ can be derived from the real part of the cross-spectrum between the pressure perturbation, p', and $U_{||}$. However, instead of computing wave momentum fluxes by the method described in Vincent and Hertzog (2014) we use a more direct estimate. In general, the SPB response to an isopycnic surface disturbed by a gravity wave will not be in-phase with the wave (Nastrom, 1980; Vincent & Hertzog, 2014), but at intrinsic frequencies much less than N, the phase shift is negligible and the balloon follows the isopycnal surface. In this limit, the vertical wave displacement ζ' can be derived directly using

$$\zeta' = \frac{\zeta_b}{|Z_{EDS}|} \tag{6}$$

where ζ_b is the vertical displacement of the balloon from its equilibrium density surface (EDS). Z_{EDS} is a factor that depends on the prevailing meteorological conditions, and given by

$$|Z_{EDS}| = \frac{2N^2}{3\omega_B^2} = \frac{\left(\frac{d\overline{T}}{dz} + \frac{g}{c_p}\right)}{\left(\frac{d\overline{T}}{dz} + \frac{g}{R_a}\right)}. \tag{7}$$

R_a is the atmospheric gas constant. Using the temperature profile shown in Fig 3b with $d\overline{T}/dz = 4.8$ K/km at the SPB float altitude, gives $|Z_{EDS}| = 0.37$ or $\zeta' = 2.68\,\zeta_b$. Hence,

the GW vertical velocity perturbation is $w' = \partial\zeta'/\partial t$. Computing the zonal and meridional fluxes $\overline{u'w'}$ and $\overline{v'w'}$ then resolves the θ ambiguity in the horizontal propagation direction. The horizontal wavenumber is given by $k_h = \hat{\omega}/\hat{c}$, with components ($k$, l), and the vertical wavenumber is derived from equation (4). The ground-based frequency ω and period τ_o are then found via the Doppler shift equation, $2\pi/\tau_o = \omega = \hat{\omega} + k\bar{u}\cos\theta + l\bar{v}\sin\theta$ where $\bar{u}$ and $\bar{v}$ are the mean wind components at the float altitude (Vincent & Hertzog, 2014). The ground-based phase speed, c_o, and its direction θ_o, are derived as described by Boccara et al. (2008). Table 2 summarizes the results.

Table 2. Gravity wave parameters derived from SPB observations. u'_{rms} is the computed horizontal perturbation amplitude, $\rho_o\overline{u'_{||}w'}$ is the vertical flux of horizontal momentum, $\hat{c}$, (c_o) and θ (θ_o) are the intrinsic (ground-based) phase speed and azimuth of propagation (anticlockwise from east). λ_h and λ_z are the respective horizontal and vertical wavelengths, and τ_o the ground-based period.

Parameter	1	2
u'_{rms} (ms^{-1})	3.2	2.2
$\rho_o\overline{u'_{||}w'}$ (mPa)	4.3	0.7
$\hat{c}$ (ms^{-1})	11.4	22.1
θ (deg)	203	341
λ_h (km)	972	5375
λ_z (km)	2.7	5.2
τ_o (day)	1.75	3.14
c_o (ms^{-1})	6.4	19.8
θ_o (deg)	203	341

With these basic wave parameters it is now possible to examine the vertical and horizontal propagation of the wave packets using gravity wave ray tracing techniques. The basic, 7-day average, atmospheric profiles used are shown in Fig. 3. The methodology follows Marks and Eckermann (1995), which allows both the ray path and the wave action, and hence wave amplitude, to be derived as a function of latitude, longitude, height and time. Figure 5 shows the horizontal paths (Fig. 5c) of the two wave packets ema-

nating from their respective locations, together with plots of the vertical profile of their respective intrinsic phase speeds and vertical wavelengths (Figs. 5a,b).

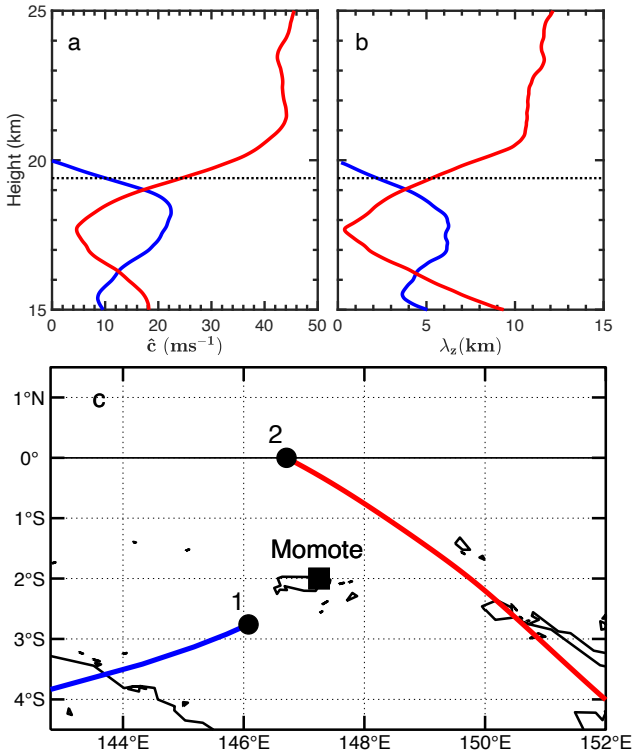

Figure 5. (a) Vertical profiles of GW intrinsic phase speed, $\hat{c}$, for packets 1 (blue) and 2 (red). (b) Profiles of vertical wavelengths, λ_z. (c) Horizontal projection of ray paths for heights above the balloon float altitude. In (a) and (b) the dotted line shows the mean float altitude of the SPB.

It is evident from Fig 5 that both $\hat{c}$ and λ_z become small for packet 2 at heights between 17 and 18 km. This may indicate the source height for this wave is in the vicinity of the tropical tropopause near 17 km because a wave propagating from below would not likely penetrate this layer without breaking. In contrast, packet 1 has non-negligible phase speeds and wavelengths at heights below the SPB level, but these values rapidly decrease above the float altitude. Near 20 km the wave encounters a critical level where the phase speed matches the background wind. A critical level so close to the balloon level calls into question the accuracy of the inferred wave parameters as $\hat{\omega} \to f$ (Fritts & Alexander, 2003). The ray path was terminated after a few hours, when the vertical wavelength had decreased to less than 0.5 km.

Two height regimes are appropriate when considering Momote radiosonde and SPB GW comparisons. Reverse ray tracing for packet 1 (not shown) suggests that it passed close to Momote a few hours ahead of the time it was observed by the SPB *i.e.* about 00 UT on day 117. It also appeared to emanate from somewhere in the altitude region above 15 km. The wave amplitude at the time of closest approach to Momote is computed to be $\sim$2.75 ms^{-1}. Conversely, the ray for packet 2 passes within about 160 km of Momote some 2-3 hr after launch *i.e.* closest approach at $\sim$21 UT on day 119 (April 29). At this time, the altitude of the packet is near 20 km and the computed horizontal perturbation amplitude is about 2.5 ms^{-1}. These results indicate that packet 1 influences the radiosonde observations at heights between 15 and 20 km near day 117, while the effects of packet 2 will be felt at heights at and above 20 km, particularly near day 120. However, packet 2 in particular has a large horizontal scale and may be present across the region covered by the radiosonde site and the balloon path for many days and also at significant depths below the SPB float altitude.

3.2 Momote Radiosonde GW Observations

As a radiosonde ascends it acts as a passive tracer of GW motions, giving a vertical 'snapshot' of the wavefield, provided the ascent rate is greater than a few ms^{-1} and the background winds are less than 10 times the ascent rate (Gardner & Gardner, 1993). The background state is often determined and removed by fitting low-order polynomials to tropospheric or stratospheric wind and temperature profiles (Allen & Vincent, 1995; Wang & Geller, 2003). Our focus is on the region around the tropopause and lower stratosphere where there is a large shear in $\overline{u}$, and polynomial fits lead to large discontinuities at the boundaries of the residual profiles. Accordingly, a somewhat different approach is used for background removal. Seven-day running means of the wind and temperature components are subtracted from the individual profiles to get the GW-induced perturbations. This method is akin to the technique used by Kim and Alexander (2015) who studied tropical wave temperature perturbations as a function of height derived from Western Pacific radiosonde observations.

The leftmost panels in Figure 6 show residual profiles for a thirteen-day period centered on day 120. Wavelike perturbations are evident in all profiles, showing downward phase progression, indicative of upward energy propagation. These features are brought out in a different way in image plots of the wind and temperature perturbations (Right:

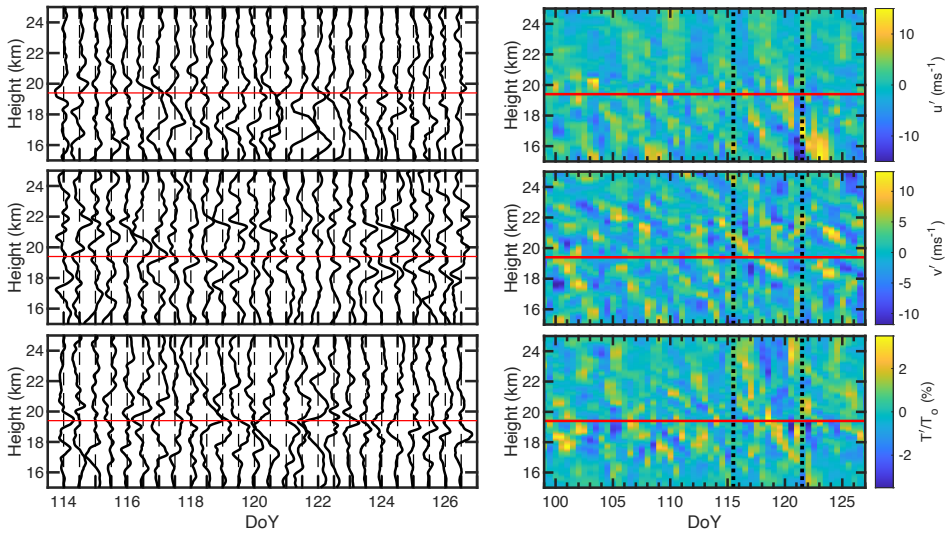

Figure 6. Left Panels: Profiles of u' (top), v' (middle) and T'/T_o (bottom) for individual radiosonde soundings made at Momote between days 114 and 127 (see text for details). The spacing between profiles is equivalent to 15 ms^{-1} for the wind components and 3.75% for the fractional temperature perturbations. Right Panels: Image plots for u' (top), v' (middle) and T'/T_o (bottom) for days 99 to 127. The vertical lines indicate the period of closest approach to Momote and the red lines in both panels show the mean altitude of the SPB.

.

Figure 6). The height-time phase tilts suggest dominant GW motions with ground-based periods of a few days and increasing vertical wavelengths with increasing height. It should be remembered that the 12-hr sampling rate means a 24-hr Nyquist period, so waves with periods less than 24 hr will be difficult to see in the time series, but longer period waves should be clearly visible. Hence, the wave field will be dominated by waves with periods of a day or longer.

3.3 Stokes Parameters

Inertia-gravity wave motions are elliptically polarized as a function of height. The Stokes-parameters method is a way to analyse wave observations made using a variety of sounding techniques in order to quantify the amplitudes and polarization (Vincent & Fritts, 1987; Eckermann & Vincent, 1989; Vincent et al., 1997; Vincent & Alexander, 2000; Schöch et al., 2004). Eckermann (1996) provides an extensive analysis of the technique as applied to hodographs of wind perturbations (u', v') composed of a partially polar-

ized wave field that contains a coherent wave with peak amplitude $U_o = (u_o, v_o)$ plus unpolarized isotropic fluctuations with variance $\overline{u^2_{noise}} + \overline{v^2_{noise}}$. Following Eckermann (1996), the parameters are defined as

$$I = \frac{1}{2}(\overline{u_o^2} + \overline{v_o^2}) + \overline{u^2_{noise}} + \overline{v^2_{noise}} = (\overline{u'^2} + \overline{v'^2}) \quad (8)$$

$$D = \frac{1}{2}(\overline{u_o^2} - \overline{v_o^2}) = \overline{u'^2} - \overline{v'^2} \quad (9)$$

$$P = \overline{u_o v_o \cos\delta} = 2\overline{u'v'} \quad (10)$$

$$Q = \overline{u_o v_o \sin\delta} \quad (11)$$

where the overbars denote time/height averaging of the perturbations. I is a measure of the kinetic energy associated with the wave field, while the other parameters can be used to determine factors of the polarization ellipse, such as the axial ratio AR which is the ratio of the major to minor axis or equivalently $U_{||}$ to $U_\perp$ where $U_{||}$ and $U_\perp$ are the wind components parallel and perpendicular to the major and minor axes. AR is related to the ratio of $\hat{\omega}$ to f (Vincent & Fritts, 1987; Eckermann & Vincent, 1989). The degree of polarization, dp, which quantifies the fractional contribution of any coherent wave motion to the total velocity variance is defined as

$$dp = \frac{(D^2 + P^2 + Q^2)^{1/2}}{I}, \quad (12)$$

Following Eckermann and Vincent (1989) we compute the Stokes parameters in vertical wavenumber space.

Since it is not possible to derive a unique direction of horizontal propagation from the Stokes analysis, this parameter was deduced by computing covariances between the wind and temperature perturbations. The intrinsic direction is given by

$$\alpha = \tan^{-1}(\overline{v'\hat{T}}_{+90}, \overline{u'\hat{T}}_{+90}) \quad (13)$$

where the overbars indicate averages in height and $\hat{T}_{+90}$ is the Hilbert-transform of the temperature perturbations normalized by the background temperature (Vincent et al., 1997).

3.3.1 Packet 1

Three factors need to be considered. Firstly, packet 1 has short duration (∼1 day), secondly, reverse ray tracing indicates that its closest approach to Momote occurs near 00 UT on day 117 and thirdly, Figure 5 shows that only the 15-20 km height range need

Table 3. Summary of Stokes parameters for packet 1 computed from three radiosonde flights centered on day 117 and covering the height range 15-20 km. $\overline{X}$ is the mean value of each parameter and $\overline{\Delta X}$ is the associated mean absolute deviation (see text).

Parameter	$\overline{X}$	$\overline{\Delta X}$
I (m^2s^{-2})	35	11
dp	0.59	0.02
$\|AR\|$	7.0	3.7
α (deg)	249	42

be considered. To accommodate the short duration, Stokes parameters were computed using just 3 radiosonde flights (days 116.5, 117.0 and 117.5). Results are summarized in Table 3, which shows the mean values ($\overline{X}$) for four parameters that encapsulate the whole analysis. The mean absolute deviation ($\overline{\Delta X} = \Sigma(|X_i - \overline{X}|)/3$) is used to estimate the variability in the mean value.

The values of I and dp together indicate that the coherent wave has an amplitude $\sqrt{dp \times I} = U_{rms} \sim 4.5$ ms^{-1}. D has a value ~ 5 m^2s^{-2}, so u_o and v_o are estimated to be about 5 and 4 ms^{-1}, respectively. The relatively large value of $|AR|$ implies near linear polarization, consistent withthe medium-frequency approximation (sec. 3.1). The horizontal direction of propagation α has quite a large deviation, but is consistent with overall propagation toward the south-west. This is in accord with the value of about 200° derived from the SPB observations (Table 2) and the ray tracing results (Fig 5). We also note the zonal wind and temperature profiles on DOY 117 in Fig. 6a show a wavelength close to ∼5 km below the balloon height and the apparent disappearance of this wave above 20 km, consistent with the identification of a critical level near 20 km determined from the ray trancing (Fig. 5a).

3.3.2 Packet 2

The vertical extent of packet 2 is unknown, but given its large horizontal wavelength and long duration it is assumed that the packet will have a considerable depth. A height range of 18 to 25 km was chosen to study its characteristics since N^2 is nearly constant over this height range (Fig. 3), although the background wind shows increasing west-

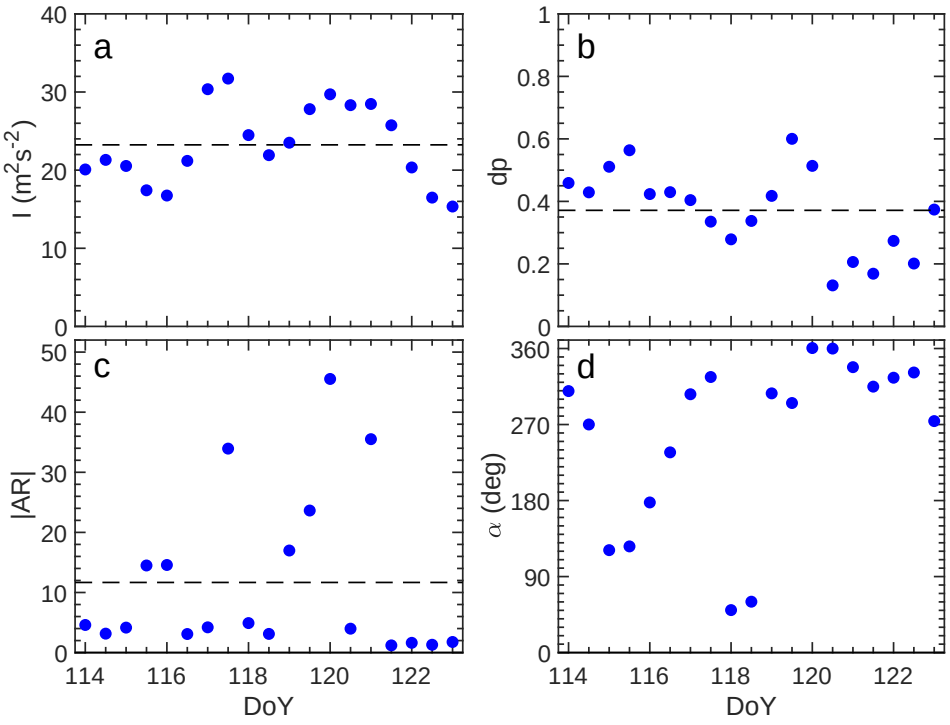

Figure 7. Values of (a) the total wind variance, I, (b) degree of polarization, dp, (c) modulus of the axial ratio, $|AR|$ and (d) horizontal direction of travel, α, derived using Stokes analyses of the radiosonde data taken every 12 hours over the 18-25 km height range at Momote. The dashed lines show the relevant mean values from days 114 to 123.

ward flow with height. The results from the Stokes analysis are summarized in Figure 7. To focus on the longer term (several day) features, short term, intra-diurnal, variations in basic parameters (I, D, P and Q) were reduced using a 3-point running-mean low-pass filter with weights (1/4, 1/2, 1/4) in time.

Packet 2 approaches closest to Momote during the interval day 118 to 122. Figure 7 shows that the mean value and standard error for the total variance is $I \sim 26\pm$ 1 m^{2}s^{-2}, for $dp \sim 0.32 \pm 0.06$, $|AR| \sim 15 \pm 6$ and for the direction of propagation is $\alpha \sim 348° \pm 15°$, anticlockwise from east *i.e.* propagation to the southeast. The large value of $\overline{|AR|}$ implies near linearity of the wave motions ($\hat{\omega} >> f$) and the combination of I and dp suggests that the coherent wave component has an amplitude of $U_{rms} \sim$ 3 ms^{-1}. Comparison with the amplitude and direction of wave motion estimated from the SPB observations (Table 2, column 2) shows good agreement with the values derived from the radiosonde observations. Finally, It should be noted that recalculating the Stokes

parameters over different height ranges, such as 16-23 km, do not change the results significantly, which is likely due to the fact that the Stokes results will be most sensitive to altitudes $\sim 18-20$ km, where this wave has a low intrinsic frequency. We also note that the wave anomalies observed in the radiosonde profiles between DOY 118-122 in Fig. 6 also show short vertical wavelength structure near the tropopause transitioning to much deeper structure above, which is consistent with the Stokes analysis and the ray tracing results (Fig. 5b).

4 Summary and Discussion

The close approach of a superpressure balloon and 6-day dwell time to a nearby radiosonde site in the near-equatorial Western Pacific allows a detailed study of gravity waves by providing complementary information on vertical wave structure. The SPB provides high time resolution measurement in an intrinsic reference frame as function of time and space, but only at a fixed altitude. The radiosonde measurements provide twice-daily snapshots of the wave field as a function of height, but only at a single location. Sonde-derived wind and temperature fields also provide context for wave propagation in the vertical. At the time of the SPB passage near Momote the zonal winds at the 19.4 km float altitude transitioned from the eastward to the westward phase of the QBO.

We focus here on two large amplitude GW packets that have intrinsic periods near 1 day and 3 days, respectively. Wave properties derived from an S-transform analysis of the SPB data are supported by a Stokes analysis of the radiosonde observations. Both waves have short vertical wavelengths of a few km in the lower stratosphere but both have large horizontal scales, which in the case of the near 3-day wave is estimated to be over five thousand km. Vertical propagation of the shorter period, westward propagating, wave, is inhibited by a critical level at 20 km, but the longer period, eastward propagating, wave is able to travel into the middle stratosphere. These case studies allow us to estimate the impact of single wave events on wave driving of the QBO and on tropical cold-point temperatures.

An important attribute of the SPB observations is that they can provide estimates of the GW momentum flux for each packet (Table 2) and hence, via equation (2) allow the drag forces to be estimated if the height region over which each of the waves are dis-

sipated is known. However, (2) by itself is inadequate to assess the impact of the waves on the QBO; one must also consider the duration and the scale of the forcing compared to the zonal mean. For these long period wave events, we can assume they are acting on a time scale of at least ∼1 day, and in the case of packet 2 several days and because for these large scale waves the force is distributed over very large horizontal regions. Accordingly, an additional parameter, the area factor, A_{fac}, is required. This is simply defined as the area of wave packet dissipation normalized by the area of the zonal mean, which in turn can be simplified to be the zonal length of the wave packet dissipation area divided by the circumference of the earth. Assuming that the packet size is approximately 2-3 times the horizontal wavelength, λ_h in km, then $A_{fac} \sim 2 - 3 \times \lambda_h/40000$. Hence the zonal mean force is

$$\overline{F}_{zonal} = \overline{F}_{local} \times A_{fac} \tag{14}$$

where F_{local} is given by Eqn. (2).

For packet 1, the momentum flux = 4.3 mPa at the SPB float altitude and the wave has a λ_h = 970 km. Assuming the dissipation occurs over $\Delta z \sim 600$ m and $\rho_o = 0.1$ kg m^{-3} then $\overline{F}_{local} \sim -6.2$ ms^{-1}day^{-1} while $A_{fac} \sim 2-3\times(970/40000)$, so the zonal mean force is $\overline{F}_{zonal} \sim 0.3 - 0.5$ ms^{-1}day^{-1} and acts for about one day.

Based on time series of the QBO in April-May 2010, packet 2 would encounter its own critical level at a height near 30 km or 10 hPa where the density is $\rho_o = 0.022$ kg m^{-3}. If the eastward flux is dissipated over a height range of $\Delta z \sim 2$ km then $\overline{F}_{local} \sim$ 1.5 ms^{-1}day^{-1}. In this case the area factor is $A_{fac} \sim 2 - 3 \times (5350/40000) \sim 0.27 -$ 0.40, so the zonal mean force is estimated to be $\overline{F}_{zonal} \sim 0.4 - 0.6$ ms^{-1}day^{-1} and it will act for several days. Despite the smaller peak flux, packet 2 has a bigger impact than packet 1 because it dissipates at a higher altitude, where the density is lower, and its large scale and long duration means that its forcing is exerted over longer temporal and spatial scales.

To place these results in context, we note that Jewtoukoff et al. (2013) derived the average momentum fluxes for waves with periods shorter than a day for SPB flights 1 and 2 in the tropics. They reported average fluxes of about 5 mPa, but found the fluxes to be highly intermittent; peak values of several hundreds mPa could be reached on timescales of an hour or so. These high events were mostly tied to both convective sources. In terms of individual packets, a similar large-scale gravity wave was observed using a cluster of

radiosonde observations near Darwin Australia (Evan & Alexander, 2008). Their case study found a wave with a 2-day period and horizontal wavelength of ∼7000km propagating southeastward, but the analysis suggested much smaller momentum fluxes than we observe here.

The total zonal-mean force needed to drive the QBO is roughly 0.3-1.0 $ms^{-1}day^{-1}$ depending on altitude and phase of the QBO, and contributions from Kelvin waves roughly half of that during the westerly phase of the QBO (M. J. Alexander & Ortland, 2010). The wave events we observe here near Momote are contributing a substantial fraction (50-100%) of the total wave force needed to drive the QBO, albeit for only for a few short days of time. If one assumes similar waves occur fairly continuously at other locations and times, then we could easily account for the necessary gravity wave driving of the QBO with gravity waves of this type. Of particular note, is the fact that the 1-day wave imparts a significantly strong force near 20 km in the lower stratosphere. Gravity wave parameterizations tend to give much weaker forces at these low levels, and instead tend to contribute primarily to the upper levels of the QBO. In fact this tendency for parameterized gravity wave drag to be weak in the lower stratosphere may be why most models simulate weaker than observed QBO amplitudes in the lower stratosphere (Bushell et al., 2020).

Observations show that short vertical scale waves also cause temperature variations near the tropical tropopause with impacts on cold point temperatures (CPT), cirrus cloud occurrence, changes in stratospheric water vapor, turbulent layers, and vertical mixing (Kim & Alexander, 2015; Kim et al., 2016; Jensen et al., 2017; Podglajen et al., 2017). In particular, radiosondes launched from tropical sites in the Western Pacific indicate that collectively, tropical waves reduce the average CPT by 1.6 K relative to seasonal means, leading to stratospheric water vapor concentrations ∼25% lower than would occur in the absence of tropical waves (Kim & Alexander, 2015), and with associated surface temperature impacts (Solomon et al., 2010). Radiosonde profiles from Momote suggest that the two wave events in this study lowered the CPT by 2-3 K below the 7-day running mean temperature.

At the time of submission of this manuscript, a new set of tropical superpressure balloon measurements are currently being made and analyzed as part of the Strateole-2 test campaign, with balloon launches in late November to early December 2019. Haase

et al. (2018) describe the plans for this campaign, which includes measurements from several high-resolution vertical profiling instruments. These data have yet to be fully analyzed, but our study provides an example of the additional information on tropical waves that can be obtained by combining high-vertical resolution profile measurements with superpressure balloon *in situ* wind and pressure measurements..

Acknowledgments

The SPB data used in this study described in (Podglajen et al., 2016) can be obtained at ftp://ftp.lmd.polytechnique.fr/hertzog/balloon/Pre-Concordiasi/tsen/ and associated documentation is here: ftp://ftp.lmd.polytechnique.fr/hertzog/balloon/Pre-Concordiasi/doc/. The contact is Albert Hertzog (albert.hertzog@lmd.polytechnique.fr). The Momote radiosonde data can be obtained from https://doi.org/10.1594/PANGAEA.841474 (Long, 2015). MJA was supported by grants from the National Science Foundation, award numbers 1642644 and 1642246. MJA also thanks the University of Adelaide for travel support under the George Southgate Visiting Fellowship scheme. Helpful comments by Dr Martina Bramberger on a draft of this paper are much appreciated.

References

Alexander, M. J., Gille, J., Cavanaugh, C., Coffey, M., Craig, C., Dean, V., ... Nardi, B. (2008). Global estimates of gravity wave momentum flux from high resolution dynamics limb sounder (HIRDLS) observations. *J. Geophys. Res.*, *113*(D15S18), doi:10.1029/2007JD008807.

Alexander, M. J., & Holt, L. A. (2019). The Quasi-Biennial Oscillation and its influences at the surface. *US Clivar Variations*, *17*(1), 20-26. doi: 10.5065/q3jb-9642

Alexander, M. J., & Ortland, D. A. (2010). Equatorial waves in High Resolution Dynamics Limb Sounder (HIRDLS) data. *J. Geophys. Res. Atmos.*, *115*(D24111). doi: 10.1029/2010JD014782

Alexander, S. P., Tsuda, T., Kawatani, Y., & Takahashi, M. (2008). Global distribution of atmospheric waves in the equatorial upper troposphere and lower stratosphere: COSMIC observations of wave mean flow interactions. *J. Geophys. Res.*, *113*(D24), D24115. doi: 10.1029/2008JD010039

Allen, S. J., & Vincent, R. A. (1995). Gravity wave activity in the lower atmosphere:

Seasonal and latitudinal variations. *J. Geophys. Res.*, *100*, 1327-1350.

Boccara, G., Hertzog, A., Vincent, R. A., & Vial, F. (2008). Estimation of gravity-wave momentum fluxes and phase speeds from quasi-Lagrangian stratospheric balloon flights. 1: Theory and simulations. *J. Atmos. Sci.*, *65*, 3042–3055.

Boer, G. J., & Hamilton, K. (2008). QBO influence on extratropical predictive skill. *Climate Dynamics*, *31*(7), 987–1000. doi: 10.1007/s00382-008-0379-5

Bushell, A. C., Anstey, J. A., Butchart, N., Kawatani, Y., Osprey, S. M., Richter, J. H., ... Yukimoto, S. (2020). Evaluation of the Quasi-Biennial Oscillation in global climate models for the SPARC QBO-initiative. *Q. J. R. Meteorol. Soc.*, (in press). doi: 10.1002/qj.3765

Butchart, N., Anstey, J. A., Hamilton, K., Osprey, S., McLandress, C., Bushell, A. C., ... Yukimoto, S. (2018). Overview of experiment design and comparison of models participating in phase 1 of the SPARC Quasi-Biennial Oscillation initiative (QBOi). *Geoscientific Model Development*, *11*(3), 1009-1032. doi: 10.5194/gmd-11-1009-2018

Eckermann, S. D. (1996). Hodographic analysis of gravity waves: Relationships among stokes parameters, rotary spectra and cross-spectral methods. *J. Geophys. Res.-Atmospheres*, *101*, 19169–19174. doi: 10.1029/96JD01578

Eckermann, S. D., & Vincent, R. A. (1989). Falling sphere observations of anisotropic gravity wave motions in the upper stratosphere over Australia. *Pure Applied Geophys.*, *130*, 510–532.

Evan, S., & Alexander, M. J. (2008). Intermediate-scale tropical inertia gravity waves observed during the TWP-ICE campaign. *J. Geophys. Res.-Atmospheres*, *113*. doi: 10.1029/2007JD009289

Fritts, D. C., & Alexander, M. J. (2003). Gravity wave dynamics and effects in the middle atmosphere. *Rev. Geophys.*, *41*, 1003, doi:10.1029/2001RG000106.

Gardner, C. S., & Gardner, N. F. (1993). Measurement distortion in aircraft, space shuttle, and balloon observations of atmospheric density and temperature perturbation spectra. *J. Geophys. Res.*, *98*, 1023–1033. doi: 10.1029/92JD02025

Garfinkel, C., I, Schwartz, C., Domeisen, D. I., V, Son, S.-W., Butler, A. H., & White, I. P. (2018). Extratropical atmospheric predictability from the Quasi-Biennial Oscillation in subseasonal forecast models. *J. Geophys. Res.-Atmospheres*, *123*(15), 7855-7866. doi: 10.1029/2018JD028724

Geller, M. A., & Gong, J. (2010). Gravity wave kinetic, potential, and vertical fluctuation energies as indicators of different frequency gravity waves. *J. Geophys. Res. Atmos.*, *115*, D11111. doi: 10.1029/2009JD012266

Giorgetta, M. A., Manzini, E., & Roeckner, E. (2002). Forcing of the quasi-biennial oscillation from a broad spectrum of atmospheric waves. *Geophys. Res. Lett.*, *29*(8), 86-1–86-4. doi: 10.1029/2002GL014756

Gong, J., & Geller, M. A. (2010). Vertical fluctuation energy in United States high vertical resolution radiosonde data as an indicator of convective gravity wave sources. *J. Geophys. Res. Atmos.*, *115*, D11110. doi: 10.1029/2009JD012265

Haase, J. S., Alexander, M. J., Hertzog, A., Kalnajs, L., Deshler, T., Davis, S. M., ... Venel, S. (2018). Around the world in 84 days. *Eos*, *99*. doi: 10.1029/2018EO091907

Hertzog, A., Alexander, M. J., & Plougonven, R. (2012). On the intermittency of gravity wave momentum flux in the stratosphere. *J. Atmos. Sci.*, *69*(11), 3433-3448. doi: 10.1175/JAS-D-12-09.1

Hertzog, A., Boccara, G., Vincent, R. A., Vial, F., & Cocquerez, P. (2008). Estimation of gravity-wave momentum fluxes and phase speeds from quasi-lagrangian stratospheric balloon flights. 2: Results from the Vorcore campaign in Antarctica. *J. Atmos. Sci.*, *65*, 3056–3070. doi: 10.1175/2008JAS2710.1

Hertzog, A., Vial, F., Mechoso, C. R., Basdevant, C., & Cocquerez, P. (2002). Quasi-Lagrangian measurements in the lower stratosphere reveal an energy peak associated with near-inertial waves. *Geophys. Res. Lett,*, *29*(8), 701–704. doi: 10.1029/2001GL014083

Holt, L. A., Alexander, M. J., Coy, L., Molod, A., Putman, W., & Pawson, S. (2016). Tropical waves and the quasi-biennial oscillation in a 7-km global climate simulation. *J. Atmos. Sci.*, *73*. doi: 10.1175/JAS-D-15-0350.1

Holt, L. A., Lott, F., Garcia, R. R., Kiladis, G. N., Cheng, Y.-M., Anstey, J. A., ... Yukimoto, S. (2020). An evaluation of tropical waves and wave forcing of the QBO in the QBOi models. *Q. J. R. Meteorol. Soc.*, (In Press). doi: 10.1002/qj.3827

Jensen, E. J., Pfister, L., Jordan, D. E., Bui, T. V., Ueyama, R., Singh, H. B., ... Pfeilsticker, K. (2017). The NASA Airborne Tropical Tropopause Experiment: High-altitude aircraft measurements in the tropical Western Pa-

cific. *Bulletin of the American Meteorological Society*, *98*, 129-143. doi: 10.1175/BAMS-D-14-00263.1

Jewtoukoff, V., Plougonven, R., & Hertzog, A. (2013). Gravity waves generated by deep tropical convection: estimates from balloon observations and mesoscale simulations. *J. Geophys. Res.*, *118*, 9690–9707. doi: 10.1002/jgrd.50781

Kawatani, Y., & Hamilton, K. (2013). Weakened stratospheric quasibiennial oscillation driven by increased tropical mean upwelling. *Nature*, *497*(7450), 478–481. doi: 10.1038/nature12140

Kim, J.-E., & Alexander, M. J. (2015). Direct impacts of waves on tropical cold point tropopause temperature. *Geophys. Res. Lett.*, *42*(5), 1584-1592. doi: 10.1002/2014GL062737

Kim, J.-E., Alexander, M. J., Bui, T. P., Dean-Day, J. M., Lawson, R. P., Woods, S., ... Jensen, E. J. (2016). Ubiquitous influence of waves on tropical high cirrus clouds. *Geophys. Res. Lett.*, *43*(11), 5895-5901. doi: 10.1002/2016GL069293

Lane, T. P., Reeder, M. J., & Guest, F. M. (2003). Convectively generated gravity waves observed from radiosonde data taken during MCTEX. *Q. J. R. Meteorol. Soc.*, *129*, 1731–1740. doi: 10.1256/qj.02.196

Lim, Y., Son, S.-W., Marshall, A. G., Hendon, H. H., & Seo, K.-H. (2019). Influence of the QBO on MJO prediction skill in the subseasonal-to-seasonal prediction models. *Climate Dynamics*, *53*(3-4), 1681-1695. doi: 10.1007/s00382-019-04719-y

Long, C. (2015). *Radiosonde measurements from station Momote (2010-01).* PANGAEA. Retrieved from `https://doi.org/10.1594/PANGAEA.841567` doi: 10.1594/PANGAEA.841474

Marks, C. J., & Eckermann, S. D. (1995). A three-dimensional nonhydrostatic ray-tracing model for gravity waves: Formulation and preliminary results for the middle atmosphere. *J. Atmos. Sci.*, *52*, 1959–1984.

Marshall, A. G., Hendon, H. H., & Son, S.-W. (2017). Impact of the quasi-biennial oscillation on predictability of the Madden–Julian oscillation. *Clim. Dyn.*, *49*(4), 1365—1377. doi: https://doi.org/10.1007/s00382-016-3392-0

Murphy, D. J., Alexander, S. P., Klekociuk, A. R., Love, P. T., & Vincent, R. A. (2014). Radiosonde observations of gravity waves in the lower stratosphere

over Davis, Antarctica. *J. Geophys. Res. Atmos.*, *119*, 11,973–11,996. doi: 10.1002/2014JD022448

Nastrom, G. D. (1980). The response of superpressure balloons to gravity waves. *J. Applied Meteor.*, *19*, 1013–1019.

Podglajen, A., Bui, T. P., Dean-Day, J. M., Pfister, L., Jensen, E. J., Alexander, M. J., ... Randel, W. J. (2017). Small-scale wind fluctuations in the tropical tropopause layer from aircraft measurements: Occurrence, nature, and impact on vertical mixing. *J. Atmos. Sci.*, *74*, 3847-3869. doi: 10.1175/JAS-D-17-0010.1

Podglajen, A., Hertzog, A., Plougonven, R., & Legras, B. (2016). Lagrangian temperature and vertical velocity fluctuations due to gravity waves in the lower stratosphere. *Geophys. Res. Lett,*, *43*(7), 3543–3553. doi: 10.1002/2016GL068148

Podglajen, A., Hertzog, A., Plougonven, R., & Žagar, N. (2014). Assessment of the accuracy of (re)analyses in the equatorial lower stratosphere. *J. Geophys. Res. Atmos.*, *119*, 11,166–11,188. doi: 10.1002/2014JD021849

Richter, J. H., Solomon, A., & Bacmeister, J. T. (2014). Effects of vertical resolution and nonorographic gravity wave drag on the simulated climate in the Community Atmosphere Model, version 5. *J. Adv. Modeling Earth Sys.*, *6*(2), 357–383. doi: 10.1002/2013MS000303

Scaife, A. A., Arribas, A., Blockley, E., Brookshaw, A., Clark, R. T., Dunstone, N., ... Williams, A. (2014). Skillful long-range prediction of European and North American winters. *Geophys. Res. Lett,*, *41*(7), 2514–2519. doi: 10.1002/2014GL059637

Schöch, A., Baumgarten, G., Fritts, D. C., Hoffmann, P., Serafimovich, A., Wang, L., ... Schmidlin, F. J. (2004). Gravity waves in the troposphere and stratosphere during the MaCWAVE/MIDAS summer rocket program. *Geophys. Res. Lett.*, *31*. doi: 10.1029/2004GL019837

Smith, D. M., Scaife, A. A., Eade, R., & Knight, J. R. (2016). Seasonal to decadal prediction of the winter North Atlantic Oscillation: emerging capability and future prospects. *Q. J. R. Meteorol. Soc.*, *142*(695), 611-617. doi: 10.1002/qj.2479

Solomon, S. K., Rosenlof, K. H., Portman, R. W., Daniel, J. S., Davis, S. M., San-

ford, T. J., & Plattner, G. K. (2010). Contributions of stratospheric water vapor to decadal changes in the rate of global warming. *Science*, *327*, 1219–1223. doi: 10.1126/science.1182488

Stockwell, R. G., Mansinha, L., & Lowe, R. P. (1996). Localization of the complex spectrum: the S transform. *IEEE Transactions on Signal Processing*, *44*, 998–1001. doi: 10.1109/78.492555

Tsuda, T., Murayama, Y., Wiryosumarto, H., Harijono, S. W. B., & Kato, S. (1994). Radiosonde observations of equatorial atmosphere dynamics over Indonesia 2. characteristics of gravity waves. *J. Geophys. Res.*, *99*, 10,507–10,516.

Vial, F., Hertzog, A., Mechoso, C. R., Badevent, C., Coquerez, P., Dubourg, V., & Nouel, F. (2001). A study of the dynamics of the equatorial lower atmosphere by use of ultra-long-duration balloons 1. Planetary scales. *J. Geophys. Res. Atmos.*, *106*, 22,725–22,743.

Vincent, R. A., & Alexander, M. J. (2000). Gravity waves in the tropical lower stratosphere: An observational study of seasonal and interannual variability. *J. Geophys. Res. Atmos.*, *105*, 17971–17982. doi: 10.1029/2000JD900196

Vincent, R. A., Allen, S. J., & Eckermann, S. D. (1997). Gravity-wave parameters in the lower stratosphere. In K. Hamilton (Ed.), *Gravity Wave Processes* (pp. 7–25). Berlin, Heidelberg: Springer Berlin Heidelberg.

Vincent, R. A., & Fritts, D. C. (1987). A climatology of gravity wave motions in the mesopause region at Adelaide, Australia. *J. Atmos. Sci.*, *44*(4), 748–760. doi: 10.1175/1520-0469(1987)044⟨0748:ACOGWM⟩2.0.CO;2

Vincent, R. A., & Hertzog, A. (2014). The response of superpressure balloons to gravity wave motions. *Atmos. Meas. Tech.*, *7*, 1043–1055. doi: 10.5194/amt-7-1043-2014

Vincent, R. A., Hertzog, A., Boccara, G., & Vial, F. (2007). Balloon-borne measurements of gravity-wave momentum fluxes in the polar stratosphere. *Geophys. Res. Lett.*, *34*, L19804. doi: 10.1029/2007GL031072

Wang, L., & Geller, M. A. (2003). Morphology of gravity-wave energy as observed from 4 years (1998–2001) of high vertical resolution U.S. radiosonde data. *J. Geophys. Res.*, *108*, 4489. doi: 10.1029/2002JD002786

Wang, L., Geller, M. A., & Alexander, M. J. (2005). Spatial and temporal variations of gravity wave parameters. part I: Intrinsic frequency, wavelength,

and vertical propagation direction. *J. Atmos. Sci.*, *62*, 125–142. doi: 10.1175/JAS-3364.1

Wright, C. J., Rivas, M. B., & Gille, J. C. (2011). Intercomparisons of HIRDLS, COSMIC and SABER for the detection of stratospheric gravity waves. *Atmos. Meas. Tech.*, *4*(8), 1581–1591. doi: 10.5194/amt-4-1581-2011